Advection Dominated Accretion Flows in the Kerr Metric: II. Steady State Global Solutions

Robert Popham[1] and Charles F. Gammie[2,3]

Harvard-Smithsonian Center for Astrophysics, MS-51

60 Garden St., Cambridge, MA 02138

June 27, 1998

ABSTRACT

In a previous paper we have written down equations describing steady-state, optically thin, advection-dominated accretion onto a Kerr black hole (Gammie & Popham (1997), hereafter Paper I). In this paper we survey the numerical solutions to these equations. We find that the temperature and density of the gas in the inner part of the accretion flow depend strongly on the black hole spin parameter a. The rate of angular momentum accretion is also shown to depend on a; for a greater than an equilibrium spin parameter a_{eq} the black hole is de-spun by the accretion flow. We also investigate the dependence of the flow on the angular momentum transport efficiency α, the advected fraction of the dissipated energy f, and the adiabatic index γ. We find solutions for $-1 < a < 1$, $10^{-4} \le \alpha \le 0.44$, $0.01 \le f \le 1$, and $4/3 < \gamma < 5/3$. For low values of α and f the inner part of the flow exhibits a pressure maximum and appears similar to equilibrium thick disk solutions.

1. Introduction

In advection-dominated accretion flows (ADAFs) the accreting gas flows inward much more rapidly than it can cool. The energy released by accretion goes into heating the gas. This is in marked contrast to the usual thin accretion disk, where the radial velocity is small and the accretion energy is efficiently radiated away. If a black hole accretes via an ADAF much of the accretion energy can be carried across the horizon with the heated

---

gas, reducing the luminosity well below that of a comparable thin disk. Paper I briefly summarizes the development of advection-dominated disk theory. Over the past few years, this theory has had notable success in reproducing the observed spectra of black hole candidate systems. For a review of the theory and applications of advection-dominated disk theory, see Narayan (1997).

Early models of advection-dominated flows around black holes (Chakrabarti (1996), Nakamura *et al.*(1996), Nakamura *et al.*(1997), Chen, Abramowicz, & Lasota (1997), Narayan, Kato, & Honma (1997)) did not include a proper treatment of relativistic effects, but instead used an approximate pseudo-Newtonian potential due to Paczyński & Wiita (1980). Close to the black hole event horizon, the gas temperatures and velocities can become extremely high. This hot, rapidly rotating and infalling gas should produce important observable effects in the high-energy spectra of black hole candidates. Relativistic effects not accounted for by the pseudo-Newtonian potential are dominant in this innermost region. The character of the inner portion of the disk also depends strongly on the black hole spin a, which is not included in the pseudo-Newtonian treatment. For these reasons, it seems clear that a fully relativistic model is needed.

Recently, advection-dominated disk models have begun to include the effects of general relativity, allowing a more accurate examination of the flow close to the event horizon. Both Abramowicz et al. (1997) (AGCL) and Peitz & Appl (1997) (PA) have presented disk solutions in the Kerr metric. In Paper I, we wrote down a set of disk equations in the Kerr metric, and showed a few example solutions. Our relativistic disk equations differ in a number of respects from those of ACGL and PA. These differences are described in detail in Paper I. The main differences with ACGL are that we use a causal stress and include the relativistic enthalpy. PA also include these effects, although they use a more simplified prescription to enforce causality. Unlike PA, who use a polytropic equation of state, we solve the energy equation assuming that a constant fraction of the dissipated energy gets advected with the gas. Also, unlike ACGL and PA, we use the height prescription of Abramowicz, Lanza, & Percival (1997).

In this paper, we examine the structure of our numerical solutions for steady state flow onto a Kerr black hole in detail. In particular, we explore the effects of changing the dimensionless black hole spin a, the viscosity parameter α, the advected fraction of the dissipated energy f, and the adiabatic index γ_0 (ACGL have shown solutions for three values of a, while PA presented a more extensive set of solutions for various values of a and α). We show that there is an equilibrium spin rate for black holes accreting via ADAFs, above which the black hole will be spun down by accretion. We also show that there is a pressure maximum in the vicinity of the last stable orbit for low α solutions (cf. NKH).

Finally we show that the Bernoulli parameter can be positive in some regions of the flow, which at least suggests the possibility of a pressure-driven outflow.

To familiarize readers with our notation, we summarize our relativistic disk equations and method of solution in §2. In §3 we examine the dependence of our disk solutions on a, α, f, and γ_0. §4 demonstrates that there is an equilibrium spin rate for black holes accreting from ADAFs. We discuss the implications of our results in §5.

2. Disk Equations and Solution Method

2.1. Summary of Disk Equations

We use a relativistic version of the slim disk equations first introduced by Paczyński & Bisnovatyi-Kogan (1981) and Muchotrzeb & Paczyński (1982) to study the structure of advection-dominated accretion disks. The equations are presented in detail in Paper I, but for the reader's convenience we summarize them here. The units are such that $G = M = c = 1$, where M is the mass of the black hole.

We begin with the continuity equation:

$$4\pi r^2 \rho H_\theta V \left(\frac{\mathcal{D}}{1-V^2}\right)^{1/2} = -\dot{M}. \tag{1}$$

Here r is the Boyer-Lindquist radius, ρ is the rest mass density, $H_\theta \equiv H/r$ is the relative disk thickness, V is the radial velocity measured in a corotating frame, $\mathcal{D} \equiv 1 - 2/r + a^2/r^2$ is a relativistic correction factor, and $\dot{M}$ is the rest mass accretion rate.

The gas energy equation is

$$V \left(\frac{\mathcal{D}}{1-V^2}\right)^{1/2} \left(\frac{\partial u}{\partial T}\frac{dT}{dr} - \frac{p}{\rho}\frac{d\rho}{dr}\right) = f\Phi. \tag{2}$$

Here u is the internal energy per unit proper volume, T is a dimensionless temperature such that the pressure $P = \rho T$, Φ is the dissipation function, and $f \le 1$ is a parameter used to mock up the effects of cooling, if any. The dissipation function Φ is given in Paper I (eq. (68) and Appendix A). We also take

$$u = \rho T g(T) \equiv \rho T \left(\frac{4/(\gamma_0 - 1) + 15T}{4 + 5T}\right), \tag{3}$$

which is a good approximation to the exact relativistic equation of state for an ideal relativistic Boltzmann gas (see Chandrasekhar (1939)) when $\gamma_0 = 5/3$. Because the

accretion flow is assumed to consist of a mixture of magnetic fields and ionized plasma, γ_0 can be smaller than 5/3.

The radial momentum equation is

$$\frac{V}{1-V^2}\frac{dV}{dr} = f_r - \frac{1}{\rho\eta}\frac{dp}{dr},\tag{4}$$

where

$$f_r \equiv -\frac{1}{r^2}\frac{\mathcal{A}\gamma_\phi^2}{\mathcal{D}}(1-\frac{\Omega}{\Omega_+})(1-\frac{\Omega}{\Omega_-}).\tag{5}$$

The f_r term combines the effects of gravity and rotation, where $\mathcal{A} \equiv 1 + a^2/r^2 + 2a^2/r^3$ and $\gamma_\phi^2 = 1 + l^2(1-V^2)/(r^2\mathcal{A})$, $\Omega = u^\phi/u^t$ is the angular velocity, and $\Omega_\pm = \pm(r^{3/2}\pm a)^{-1}$. The radial acceleration, on the left-hand side, is given by the difference between f_r and the pressure gradient force, where η is the relativistic enthalpy $\eta \equiv (\rho + p + u)/\rho$.

The angular momentum conservation equation is

$$\dot{M}l\eta - 4\pi H_\theta r^2 t^r{}_\phi = \dot{M}j.\tag{6}$$

Here l is the specific angular momentum of the accreting gas, $j = const.$ is the angular momentum accretion rate per unit rest mass accreted. The remaining term gives the viscous angular momentum transport rate, where t^r_ϕ is the viscous stress. Notice that we solve for j as an eigenvalue, as do NKH and ACGL. PA prespecify j (which they label L_0) and iterate in j when they want to find a solution with a specified value of l at the outer edge of the disk. Chakrabarti (1996) also prespecifies j.

The calculation of t^r_ϕ is rather lengthy, and the reader is referred to §4 of Paper I for a full mathematical discussion. To briefly summarize the relevant physics, we begin by calculating the shear rate σ in the local rest frame of the accreting gas. This gives a complicated expression which is closely approximated by the thin disk shear rate derived by Novikov & Thorne (1973), $\sigma_{thin} = (1/2)\mathcal{A}\gamma_\phi^2 r d\Omega/dr$ (see the Appendix of Paper I for a discussion). Next we specify the relation between the turbulent shear stress and the shear rate (rate of strain). The simplest prescription is the usual Navier-Stokes form in which stress is simply proportional to rate of strain. As is well known, the resulting system of equations is acausal. To preserve causality, we use a relativistic version of a prescription that originated with Maxwell (1867) and Cattaneo (1948, 1958) and was discussed in the context of accretion disk theory by Papaloizou & Szuszkiewicz (1994) (Narayan, Loeb, & Kumar (1994) give a mathematically equivalent formulation). This modification limits the propagation of viscous effects to a finite speed c_ν, which we take to be $c_\nu = \sqrt{\alpha}c_s$ (our solutions are not sensitive to the precise value of c_ν). The viscous stress t^r_ϕ is then obtained by transforming back from the local rest frame to the Boyer-Lindquist frame.

The equation of vertical mechanical equilibrium is

$$H_\theta^2 = \frac{p}{\rho \eta r^2 \nu_z^2},$$ (7)

where ν_z is an effective vertical frequency. We adopt the expression derived by Abramowicz, Lanza, & Percival (1997) for ν_z:

$$\nu_z^2 = \frac{l^2 - a^2(\mathcal{E}^2 - 1)}{r^4},$$ (8)

where $\mathcal{E} = -u_t$ is the "energy at infinity", which is conserved along geodesics.

Finally, the inward flux of mass-energy is

$$\dot{E} = 4\pi H_\theta r^2 [-(\rho + u + p)\mathcal{E} u^r + t_t{}^r],$$ (9)

where t is the viscous stress tensor. We do not use this equation to find our solution. But when $f = 1$, $\dot{E}$ is constant with r, and $\dot{E} \simeq \dot{M}$, because $T \ll 1$ at large r. In this case equation (9) is a check on our numerical accuracy. It is generally satisfied to better than one part in 10^{-3}. For $f < 1$, however, $\dot{E}$ is not conserved, since some of the rest-mass is radiated away. Recall that $\dot{E}$ at the horizon, and not $\dot{M}$, is the true rate of change of the mass of the black hole.

2.2. Critical Points and Boundary Conditions

We set the outer edge of the ADAF at 10^4 Schwarzschild radii, or $r = 2 \times 10^4\, GM/c^2$, and the inner edge just outside the event horizon at $r = (1 + \sqrt{1 - a^2})\, GM/c^2$, where $\mathcal{D} = 0$.

At the outer edge we impose two boundary conditions: Ω and c_s must equal their values in the self-similar advection-dominated solution of Narayan & Yi (1994). We have also obtained solutions with the thin disk values for Ω and c_s at the outer edge, but our solutions adjust to the self-similar profile within a short distance of the boundary. NKH found a similar result, since their equations are essentially equivalent to ours in the non-relativistic limit. Thus the self-similar solution is the "natural" state of the flow far from the black hole, and is an appropriate outer boundary condition.

Two other conditions on the flow are provided by the requirement that the flow pass smoothly through two critical points. The first is the sonic point r_s, where $|V| \simeq c_s$. The second is the "viscous point" r_v associated with the finite propagation speed of viscous effects, where $|V| \simeq c_\nu$. Associated with each critical point are two conditions that must

be satisfied for a smooth flow, as well as one degree of freedom, the location of the critical point itself.

The final boundary condition normalizes the density (the density appears in the basic equations only in the form $d\ln\rho/dr$). For simplicity we set the normalization constant so that $\dot{M} = 1$. We now have all the boundary conditions required to solve the four first-order ordinary differential equations for V, l, ρ, and T, and to find the eigenvalue j. In particular, consistent with causality, no boundary conditions are applied at the event horizon.

2.3.   Method of Solution

We solve the system of equations listed above using a relaxation method. We solve for the structure of the flow in three radial regions: the subsonic, "sub-viscous" outer zone, where $r > r_v$, the subsonic, "super-viscous" middle zone, where $r_s < r < r_v$, and the supersonic, "super-viscous" inner zone, where $r < r_s$. We first solve the outer zone for a specified value of r_v, and then solve the middle zone for the same r_v. We compare the outer and middle zone solutions to see whether they match up at r_v; if not, we change r_v and repeat the procedure until the outer and middle solutions match up. Then, using the variable values from the middle solution at r_s as boundary conditions, we solve for the inner zone.

As is well known, our independent variable, the Boyer-Lindquist r, is ill-behaved near the horizon when $|a| \to 1$. This might raise some concerns about the numerical accuracy of our solutions. We have taken several steps to control for this, however. First, we use a fixed number of grid points in each radial region. As $a \to 1$, the sonic radius moves sharply inward, and this greatly increases our numerical resolution close to the horizon. Second, we have convergence-tested our solutions by increasing the number of grid points. No significant changes were found at increased resolution. Finally, notice that conditions close to the horizon do not influence the solutions at larger radius because our fundamental equations are causal: the solution in the inner region is obtained by integrating inward from the sonic point. In fact, many of the important parameters of the flow, such as the angular momentum accretion rate j, are fixed by conditions at and outside the sonic point.

3.   A Survey of Solutions

Here we describe the changes in our solutions that result from changes in four basic parameters: the black hole spin a, the viscosity parameter α, the advected fraction of the

dissipated energy f, and the adiabatic index γ. We begin from a base solution with $a = 0$, $\alpha = 0.1$, $f = 1$, and $\gamma = 1.4444$ (which corresponds to equipartition between gas and magnetic pressure). This solution was described in detail in Paper I, and it appears in each of the sets of solutions described below. Recall that physical units may be recovered as follows: radial velocity is Vc, angular momentum is lGM/c, density is $\rho \dot{M} G/c^3$ (since the mass accretion rate is set to 1), and temperature is $T \bar{m} c^2/k$, where $\bar{m}$ is the mean molecular weight and k is Boltzmann's constant.

It is worth pointing out immediately that the marginally stable orbit plays no special role in many of our solutions. While the sonic point r_s often lies close to the radius of the marginally stable orbit, there is no abrupt change in the character of the flow there. This is because pressure gradients play an important role in the radial structure of ADAFs; unlike thin disks, ADAFs are not in centrifugal balance.

3.1. Black Hole Spin a

We begin by examining the dependence of the accretion flow on the black hole spin parameter a. We solve for values in the range $-1 < a < 1$, allowing for the possibility of a counterrotating hole. The horizon lies at $r = 1 + (1 - a^2)^{1/2}$, i.e. at $r = 2$ for $a = 0$ and at $r = 1$ for $a = \pm 1$. The resulting profiles of ρ, V, Ω, l, T, and H/R are shown in Figure 1 for solutions with $a = -0.999$, -0.9, -0.5, 0, 0.5, 0.9, and 0.999.

Notice that changes in a have little effect far from the hole. Also, notice that in general the positive-a solutions differ from the $a = 0$ solution more than the corresponding negative-a solutions. This is especially dramatic in ρ and T: the $a = 0.999$ solution reaches very high density and temperature near the horizon, while the $a = -0.999$ solution has ρ and T at the horizon similar to the $a = 0$ solution.

The positive and negative-a solutions also show very different V profiles close to the hole. The positive-a solutions accelerate rapidly and plunge into the hole, while the negative-a solutions accelerate rapidly farther from the hole and only gradually near the hole, coasting across the horizon.

Figure 1 also shows the positions of the sonic and viscous points for each solution. The sonic and viscous points move to smaller r as a increases, as expected since the "plunge" toward the hole occurs at smaller radii. At $a = 0$, the sonic point is at $r \simeq 6.41$, close to the last stable orbit. At $a = 0.999$, it has moved in to $r \simeq 1.94$, while for $a = -0.999$ it moves out to $r \simeq 9.20$. The viscous point always lies much farther from the hole; in general $r_v \sim 4 - 5 r_s$. This is due to our setting $c_\nu^2 = \alpha c_s^2$, so that for $\alpha = 0.1$ we have $c_\nu \sim 0.3 c_s$.

The value of Ω at the horizon should be equal to $\omega \equiv 2a/(r^3 + a^2r + 2a^2)$ (denoted by a dashed line in Fig. 1) due to the effects of frame-dragging. This results in the symmetric distribution of inner Ω values between -0.5 and 0.5 seen in Fig. 1. For all but the high-a solutions, Ω shows a boundary layer-like profile, reaching a peak and then dropping rapidly to ω at the horizon. Had we plotted $\tilde{\Omega} \equiv \Omega - \omega$, the profiles for all values of a would resemble the Ω profile for $a = 0$.

The specific angular momentum $l\eta$ drops steadily as a increases. Notice that $l\eta$ includes the angular momentum associated with both the mass density and the energy density of the gas. The inner value of $l\eta$ decreases from over 3 to less than 2 as a goes from -0.999 to 0.999. The actual rate of angular momentum accretion by the hole per unit rest mass accreted is j. Values for j are generally close to the horizon values of $l\eta$. This means that the rate of viscous angular momentum transfer is very small near the horizon; however, it is not zero.

The relative disk thickness H/r also varies dramatically with a. Notice that for all values of a, H/r is smaller near the horizon, then increases to ~ 1 at large radii. Negative-a flows are much thinner than positive-a flows.

3.2. Viscosity Parameter α

Figure 2 shows a set of solutions with $\alpha = 0.001, 0.003, 0.01, 0.03, 0.1, 0.3$, all with $a = 0$, $f = 1$, and $\gamma = 1.4444$. Both the sonic and viscous points move steadily outward as α increases, since a larger α gives a larger viscosity coefficient for given c_s and H, producing larger radial velocities V. This removes more angular momentum and dissipates more energy, resulting in smaller values of $l\eta$ and higher temperatures for larger α. The higher temperature gives a larger relative disk thickness H/r, and this combined with the larger radial velocity makes the density decrease as α increases.

The density and temperature profiles show an interesting effect at low α: the development of a local maximum in density and temperature just outside the last stable orbit. This effect was also noted by NKH and CAL. The maximum becomes more pronounced as α decreases. It is faintly seen as an inflection in the density profile at $\alpha = 0.01$, but by $\alpha = 0.001$ it produces a very large, wide peak with a density 50% larger than the density at the horizon. The maximum in the temperature profile is less dramatic, but the combined effect of the two is to produce a pressure maximum which affects the dynamics of the flow. On the inner side of this pressure maximum, the pressure gradient force points inward. This inward force is balanced in part by more rapid rotation: Ω

increases as α decreases. In fact the $\alpha = 0.001$ solution even has a super-"Keplerian" rotation in a small region extending from $r \simeq 5 - 8$.

3.3. Advected Fraction f

The parameter f was introduced to mock up the effects of cooling. The case of greatest interest for modeling ADAFs is when cooling is unimportant, so $f \simeq 1$. We can reduce f so that it is much less than 1, however, and in this case we should approximately recover a thin disk, albeit with a radial temperature structure that is not consistent with any realistic cooling function.

Figure 3 shows solutions for $f = 1$, 0.3, 0.1, 0.03, 0.01. All of the solutions have $a = 0$, $\alpha = 0.1$, and $\gamma = 1.4444$. The dramatically lower temperatures in low-f solutions reduce c_s and H and thus reduce the viscous stress. As a result, this sequence of solutions strongly resembles the α sequence shown in Fig. 2. For small values of f, as for small values of α, a maximum develops in density, temperature, and pressure in the inner disk for small values of f, resulting in super-Keplerian values of Ω. The relative disk height drops as f decreases, and the removal of angular momentum is less efficient. The major difference between the two sequences is that low values of f produce much lower temperatures and higher densities than low values of α.

The low-f solutions are indeed close to a thin disk. In particular, the sonic point occurs close to the last stable circular orbit (this is true for solutions with a variety of a at low f). Also, the energy-at-infinity $\mathcal{E}$ and angular momentum l are close to their circular orbit values. Of course, this is expected due to the low temperatures of these models, so that radial pressure gradients play a negligible role. Nevertheless, it is good to see this expectation confirmed.

3.4. Adiabatic Index γ

The adiabatic index is not fixed by the temperature because some (unknown) fraction of the total pressure is contributed by the magnetic field, while the rest is contributed by gas pressure. Figure 4 shows a sequence of solutions for a range of values of $\gamma = 1.3333$, 1.4444, 1.55, 1.66. These correspond to the fraction of the pressure contributed by the gas pressure $\beta = 0$, 0.5, 0.8, 0.99, respectively. All solutions have $a = 0$, $\alpha = 0.1$, and $f = 1$.

The high-γ solutions get much hotter than the low-γ ones, increasing the effective viscosity coefficient. This produces higher velocities, larger relative disk heights, and

removes more angular momentum. As γ approaches 5/3, these effects become extreme. For example, the $\gamma = 1.66$ solution has unphysically large values of H/R.

4. Equilibrium Black Hole Spin Rates for Advection-Dominated Accretion

The black hole accretes both mass and angular momentum, so the dimensionless black hole spin parameter $a \equiv Jc/GM^2$ (J is the black hole angular momentum) changes with time. In dimensionless form,

$$\frac{da}{dt} = \dot{M}j - 2a\dot{E}, \tag{10}$$

where $\dot{E}$ is the inward flux of mass-energy. Thus if $j = 2a\dot{E}/\dot{M}$, then da/dt vanishes and the black hole has reached an equilibrium spin a_{eq}. The value of a_{eq}, if it exists, will depend on the input parameters a, α, f, and γ. Notice that when $f = 1$, as in most of the solutions presented here, $\dot{E} = const. \simeq \dot{M}$, and a_{eq} is reached when $j = 2a$.

The equilibrium spin is of considerable astrophysical interest since the observable properties of accretion flows change sharply in the neighborhood of $a = 1$. In an influential paper, Bardeen (1970) showed that a black hole accreting from a thin disk reaches $a = 1$ in a finite time. Thorne (1974) pointed out that if one takes account of the preferential accretion of angular momentum by the hole, then $a_{eq} = 0.998$. Abramowicz & Lasota (1980) suggested that even larger values of a_{eq} might still be obtained from a thick disk, based on numerical calculations that showed that the inner edge of these disks was located somewhere between the last stable orbit and the last bound orbit.

In order to calculate a_{eq}, we have obtained sequences of solutions with increasing a. As a increases, j decreases, and when $j = 2a\dot{E}/\dot{M}$ we have found a_{eq}. In Figure 5 above we show the dependence of j on a for the six values of $\alpha = 0.001, 0.003, 0.01, 0.03, 0.1, 0.3$, for which $a = 0$ solutions were shown in Fig. 1. In all cases, j decreases as a increases, and decreases faster as a approaches 1, particularly in the low-α solutions. Here $f = 1$, so a_{eq} is reached when $j = 2a$, as denoted by the dotted line. Notice that a_{eq} is quite far from $a = 1$ for high-α flows: for $\alpha = 0.3$, we have $a_{eq} \simeq 0.8$. On the other hand, for low-α flows, a_{eq} is very close to 1: for $\alpha = 0.001$, we have $a_{eq} = 0.999965$. The variation of a_{eq} with α is shown in Figure 6. For the sequence of $\alpha = 0.001, 0.003, 0.01, 0.03, 0.1, 0.3$, we find $a_{eq} = 0.999965, 0.99972, 0.9975, 0.985, 0.930, 0.806$. For $\alpha \leq 0.03$ we find the approximate relation $1 - a_{eq} \simeq 10\alpha^{1.8}$.

We also obtained sequences in a for values of f between 0.01 and 1, using $\alpha = 0.1, \gamma = 1.4444$. For $f < 1$ we no longer have $\dot{E} \simeq \dot{M}$, so the full form of equation (10) is required. We find $a_{eq} = 0.930, 0.988, 0.9984, 0.99983, 0.999979$, for

$f = 1, 0.3, 0.1, 0.03, 0.01$, respectively, as shown in Figure 6. Here again we find an approximate power-law relationship $1 - a_{eq} \simeq 0.1 f^{1.8}$.

These results have some interesting implications. If most of the mass of a black hole is accreted through an ADAF, then the hole cannot approach $a = 1$. All advection-dominated models of observed systems that have appeared in the literature have high values of $\alpha \sim 0.3$, since solutions with low α have extremely low luminosities. According to the results given above, the black holes in these systems will not be able to spin up past $a \sim 0.8$. The most dramatic effects of the black hole spin on the flow, which appear when a nears unity, will not be seen in such systems.

Of course, the accretion of photon angular momentum is not included in our calculation, but this is justified where $1 - f$ is small. In our flows, small values of f correspond to thin disks, which radiate a fraction $1 - f$ of the energy dissipated in the disk. The limiting spin a_{eq} also depends on f, and we find that flows with $f \gtrsim 0.1$ will have $a_{eq} < 0.998$, so they should stop spinning up before reaching the photon-transport limit. Flows with $f < 0.1$ have $a_{eq} > 0.998$, so here the photon-transport limit is relevant.

5.   Discussion

5.1.   Comparison to Earlier Solutions

Our disk equations differ in a number of respects from those used by other authors, as detailed in Paper I and above. Also, the solutions described above cover a wider range of parameter space than previous studies. We have found solutions over the ranges of $a = -0.99999$ to 0.99999, $\alpha = 0.0001 - 0.44$, $f = 0.01 - 1$, and $\gamma = 1.3333 - 1.66$.

Our sequence of solutions for $\alpha = 0.001 - 0.3$ resembles the solutions of NKH in many respects. We find sonic radii ranging from $r_s \simeq 4.28 - 9.41$ as α increases, similar to the range $r_s = 4.20 - 10.63$ found by NKH. Our solutions also develop pressure maxima at small values of α, as discussed below. Since NKH used the pseudo-Newtonian potential, their solutions have some unphysical properties near the horizon, which are avoided by our use of the full relativistic equations.

Our relativistic solutions with $a = 0$ produce emission spectra which are qualitatively similar to those calculated from the NKH solutions. The densities tend to be somewhat higher near the horizon in our solutions due to the inclusion of relativistic effects, and this increases the luminosity of the flow substantially. This was shown by Narayan et al.(1998), who calculated the emission spectrum of Sgr A* using the relativistic dynamical solutions

described in this paper. They were thus able to make a direct comparison between the spectrum computed from our solution and that computed from a pseudo-Newtonian solution as described by NKH. This showed that the inclusion of relativistic dynamics increased the emission by a factor of 10-100 in the infrared. Note that relativistic photon transport effects are not included in these spectra, apart from including the gravitational redshift. Also, the effects of using rotating black hole solutions have yet to be explored; however, it is clear that the substantial increases in temperature and density near the horizon in these solutions will have a dramatic effect on the emission spectrum.

ACGL presented solutions with $a = 0$, 0.5, and 0.99 for $\alpha = 0.1$, which included bremsstrahlung cooling. The shape of the $l(r)$ curves is similar to ours; however, the solutions differ in some other respects. First, the ACGL solutions have larger values of l at the inner edge of the flow. They find $l_{in} \simeq 3.2, 2.6, 1.7$ for $a = 0, 0.5, 0.99$, respectively, whereas our solutions have $l_{in} = 2.14, 1.79, 0.93$ for these same values of a. One reason for this is that their $l(r)$ curves only extend in to the Schwarzschild radius at $r = 2$, even for the $a = 0.5$ and $a = 0.99$ solutions, where the horizon sits at smaller radii. Also, in ACGL's scheme, the angular momentum eigenvalue which we call j is equal to l_{in} (or in their notation, $\mathcal{L} = \mathcal{L}_0$), whereas in our solutions, j can differ substantially from l_{in} due to viscous torques. Our values of j for these solutions are 2.62, 2.31, and 1.73, which are somewhat closer to the ACGL values. Another difference between our solutions and those of ACGL is that their solutions show a maximum in $\log c_s$ and inflections in $\log P$ close to the inner edge, whereas our solutions have $\log T$ and $\log P$ increasing smoothly all the way in to the horizon.

PA have presented the most extensive survey of solutions to date. They find two types of viscous disk solutions: "type I" solutions at low values of α ($\alpha = 0.001 - 0.045$ in the solutions shown) and "type II" solutions at high α ($\alpha \geq 0.3$ in the solutions shown). One major difference between PA's scheme and ours is that they specify the angular momentum eigenvalue j (which they call L_0) while we solve for it. Their type I solutions with α ranging from 0.01 to 0.045 all have the same value of L_0, and show great variation in their angular momentum profiles at large r, whereas our solutions tend to have rather similar values of l at large r. PA's type I solutions also have a maximum in the sound speed outside the sonic point, and the sound speed then decreases down to the horizon. This may be a consequence of their polytropic equation of state, which requires that the sound speed must decrease inward if the radial velocity increases inward more rapidly than $\sim r^{-1}$. Their lowest-α solutions at $\alpha = 0.001 - 0.008$ have a super-Keplerian region in the inner part of the disk. In the type II solutions shown by PA, the sonic point occurs far out in the flow at $r \sim 30 - 60$. This is a much larger sonic radius than in our high-α solutions: our $\alpha = 0.3$ solution has $r_s = 9.41$. According to PA, their type II solutions have the sonic point located

at an outer critical point rather than an inner critical point as the Type I solutions do.

Unlike PA, who found two types of solutions, and Chakrabarti (1996), who has found solutions where the flow goes through radial shocks, we find smooth solutions for the entire range of parameter values, and we see no evidence for sudden transitions between different types of solutions. In order to look for alternate solutions, we varied r_v and solved for the outer and middle sections of our solutions to see whether these sections would match up for an alternate value of r_v. Despite looking for alternate solutions with several choices of parameters, including low values of α, we found no additional solutions.

It is worth commenting in some detail on why our solutions are shock-free while those of Chakrabarti (1996) are not. The origin of this difference lies in how the boundary conditions are treated. The difference is most easily explained by analogy with the problem of spherical (Bondi-Hoyle) accretion. To solve the Bondi problem one specifies the density and temperature, but not the radial velocity (nor, equivalently, the accretion rate), at large distance from the accreting object. The velocity at large radius is adjusted until the flow passes smoothly through the sonic point. This velocity, or the accretion rate, is thus an eigenvalue of the problem and must be solved for self-consistently. This approach has been validated by numerically solving a realistic initial value problem and showing that it settles down to the Bondi solution. If one were to specify the radial velocity or accretion rate the flow would not generally pass smoothly through the sonic point; rather, it would shock.

Our treatment is analogous to the standard treatment of the Bondi problem, except that in our case the mass accretion rate is specified, while the angular momentum accretion rate j is the eigenvalue. It is adjusted so that the flow passes smoothly through the sonic point. Chakrabarti's approach, on the other hand, is analogous to prespecifying the mass accretion rate in the Bondi problem: he fixes j. As a result the flow does not generally pass smoothly through the sonic point and his solutions contain one or more shocks. Our intuition, and the analogy with the Bondi problem, suggest that this is not the correct approach. The issue can only be settled conclusively, however, by solving a realistic initial value problem and showing that it converges to one solution or the other. This has not yet been done.

5.2. Local Pressure Maxima

Our low-α solutions have a maximum in pressure, density, and temperature in the inner disk. Figure 7 shows density contours in the inner parts of the flow for various values of a and α. The contour plots are in the $x = r\sin(\theta), z = r\cos(\theta)$ plane, and assume that

$\rho \propto \exp(-\theta^2/(2H_\theta^2))$. These solutions resemble the low-α solutions of NKH. They are also similar to the thick disk models developed by a number of workers (see Fishbone & Moncrief (1976), Paczyński & Wiita (1980), Rees et al. (1982)). In particular they have a pressure maximum, approximately constant specific angular momentum, and a region of super-Keplerian rotation where pressure support is important. Generally the pressure maximum lies close to the last stable orbit, and the sonic point lies close to the marginally bound orbit. Our approximations are most accurate for these low-α solutions in that H/R is relatively small (see Figure 2) and the low viscosity implies a disk with relatively low turbulent velocities.

It is not entirely clear that the low-α models are relevant, however. A lower limit to the efficiency of angular momentum transport is set by the existence of the global hydrodynamic instability of Papaloizou & Pringle (1984). Simulations of the nonlinear development of the magnetorotational instability (Balbus, Gammie, & Hawley (1995)) suggest an even larger lower limit of order $\alpha \sim 0.01$. For α as large as this a pressure maximum does not develop, and the pressure increases smoothly down to the event horizon.

A new result of this study is the similarity of low-f solutions to low-α solutions. Our $f = 0.01$ and $f = 0.03$ solutions show pronounced density and pressure maxima in the same region of the flow, just outside the last stable orbit. They also have super-Keplerian rotation in this region. However, the low-f solutions have the sonic point at $r_s \simeq 5.72$ for $f = 0.03$ and at $r_s \simeq 5.85$ for $f = 0.01$, closer to the last stable orbit than the marginally bound orbit.

5.3. Bernoulli Parameter

The Bernoulli parameter Be measures the sum of the kinetic energy, potential energy, and enthalpy of the gas. Narayan & Yi (1994, 1995) pointed out that self-similar advection-dominated flows have a positive Bernoulli parameter for $f > 1/3$. The positivity of Be suggests the possibility of a pressure-driven outflow; Be is conserved for adiabatic, inviscid flows, so that gas with $Be > 0$ could flow outward adiabatically and still have positive kinetic energy at large radius.

In its relativistic form, $Be = \eta\mathcal{E} - 1$, where $\mathcal{E} \equiv -u_t$. Figure 8 shows Be for the solutions shown in Figs. 1–4, illustrating the variation of Be with radius and with a, α, f, and γ. Solutions with small values of a reach only small positive values of Be. In these solutions, Be tends to peak at $r \sim 6 - 20$, and reaches peak values of $Be < 0.01$ (see Fig. 8b,d). Solutions with a approaching unity can have substantially larger values of Be which

peak at the horizon (Fig. 8a). Solutions with $f < 1$, which radiate away a fraction $1 - f$ of the dissipated energy, have $Be < 0$. At large radii, the solution with $f = 0.3$ has Be only slightly negative, as expected from the self-similar result that ADAFs with $f > 1/3$ have $Be > 0$.

Variations in the Bernoulli parameter are directly related to the radial viscous energy flux, since the total radial flux of mass energy is conserved. We have

$$Be = \frac{\dot{E}}{\dot{M}} - 1 + \frac{t_t^r}{\rho u^r} \tag{11}$$

where $t_{\mu\nu}$ is the viscous stress tensor. Recall that $\dot{E}$ at the event horizon is the actual rate of change of the black hole mass; furthermore, $\dot{E} = const. \simeq \dot{M}$ when $f = 1$. One can show that, if S is the shear stress measured in the local rest frame of the fluid, then

$$t_t^r = -r \mathcal{D} u^\phi S. \tag{12}$$

Since $u^\phi \sim \mathcal{D}^{-1}$ at the horizon, t_t^r is finite at the horizon. Figure 9 shows the run of $-t_t^r$, the *outward* viscous energy flux, for solutions with several values of a but otherwise with the standard parameters.

The existence of a finite outward angular momentum and energy flux at the horizon suggests a violation of causality, yet our solution is manifestly causal. How can this be? It turns out that these fluxes appear because of how the flow is divided into a mean and fluctuating part. Consider a simple example: an accretion flow consisting of a turbulent, unmagnetized fluid with negligible density fluctuations. At a given event, the flow has angular momentum $l + \delta l$ and radial four-velocity $u^r + \delta u^r$. The mean flow is defined so that $\langle \delta l \rangle = 0$ and $\langle \delta u^r \rangle = 0$, where the brackets denote an average over t, θ, ϕ. Then the outward flux of angular momentum is

$$T_\phi{}^r = (\rho + u + p)(l + \delta l)(u^r + \delta u^r), \tag{13}$$

using the definition of the perfect fluid stress tensor. Averaging,

$$T_\phi{}^r = (\rho + u + p)[lu^r + \langle \delta l \delta u^r \rangle]. \tag{14}$$

The first term in brackets is due to the mean flow; the second term is what we have called the "viscous" angular momentum flux. Evidently the outward flux of angular momentum (or energy; the same considerations apply to $T_t{}^r$) appears because of how we have divided the flow into a mean and fluctuating part. Correlations in the fluctuations merely bias the angular momentum of accreting fluid elements. Causality is preserved.

5.4.   Assumptions and Limitations

Finally, it is worth offering a frank discussion of the assumptions behind our solutions and their limitations. A somewhat hidden assumption is that the accreting plasma is a two-temperature plasma with proton temperature much greater than the electron temperature. Only then will $f \simeq 1$. This can be true only if most of the "viscous" dissipation goes into the protons and there is no collective effect that efficiently couples the protons and electrons. No such effect has yet been convincingly demonstrated to exist.

The assumption that f is constant with radius is only likely to hold true if $f \simeq 1$ throughout the flow. We have nonetheless calculated solutions for constant $f < 1$ in order to illustrate the effects of a smaller value of f on the dynamical aspects of the flow. In the future, it is clear that models will need to include cooling processes and calculate f self-consistently. This task is complicated by the importance of Compton cooling in these flows, which depends not only on the local conditions at a particular radius, but also on the incident photon flux from all other radii. Thus far, cooling has been included in some detail in some models, but no model has included both a full treatment of cooling and fully relativistic dynamics.

Some additional assumptions and limitations of our solutions are tied to our treatment of angular momentum transport. For example, we have vertically averaged the flow. This should produce a reasonably reliable solution close to the midplane, but is not predictive for flow near the poles. We could produce a full axisymmetric steady-state solution, but because it is not known how turbulent angular momentum transport varies with height in the accretion flow, such an effort would not significantly improve the reliability of the solution. In addition, the flow has been assumed smooth and steady. This is likely to be true only in a time-averaged sense. In particular, if $\alpha \sim 1$, then the turbulence that transports angular momentum will be only marginally subsonic and shocks and substantial density variations are likely.

6.   Summary

We have presented steady-state solutions in the Kerr metric for advection-dominated accretion onto black holes. The solutions extend from $2 \times 10^4 GM/c^2$ down to just outside the event horizon at $(1 + \sqrt{1 - a^2})GM/c^2$. The flow passes through a sonic point and a viscous point which arises due to our use of a causal viscosity prescription. We find large variations in the character of the flow by varying the solution parameters, which include the black hole spin a, the viscosity parameter α, the advected fraction f, and the adiabatic

index γ. We find smooth solutions without shocks throughout the parameter space.

The innermost part of the flow near the horizon becomes much hotter and denser as a approaches 1. Also, the amount of angular momentum transferred to the black hole, which is an eigenvalue of our solutions, drops as a increases. The structure of the flows is sensitive to α, the efficiency of angular momentum transport. For $\alpha \lesssim 10^{-3}$, the flows exhibit a pressure maximum and an approximately constant specific angular momentum profile, similar to the "thick disk" or "ion tori" models. The same holds true for solutions with small values of f, even though the low-f solutions are geometrically thin and are similar to the classical thin disk solutions in a number of respects.

We find that an equilibrium spin rate a_{eq} exists for black holes accreting from an advection-dominated flow. This results from the decrease in the angular momentum accretion rate as a increases. At a_{eq}, the accreted angular momentum is just sufficient to counteract the effects of mass accretion and keep a constant. For large values of α and f, $a_{eq} \simeq 0.8 - 0.9$, well below the maximum value of $a \simeq 0.998$ allowed by photon transport.

REFERENCES

Abramowicz, M.A., Chen, X., Granath, M., & Lasota, J.P. 1996, ApJ, 471, 762 (ACGL)

Abramowicz, M.A., Lanza, A., & Percival, M.J. 1997, ApJ, 479, 179 (ALP)

Abramowicz, M.A., & Lasota, J.P. 1980, Acta Astronomica, 30, 35

Balbus, S.A., Gammie, C.F., & Hawley, J.F. 1995, ApJ, 440, 742

Bardeen, J.M. 1970, Nature, 226, 64

Cattaneo, C., Atti del Seminario della Universita di Modena, 3, 33

Cattaneo, C., C. R. Acad. Sci. Paris, 247, 431

Chakrabarti, S. 1996, ApJ, 471, 237

Chandrasekhar, S. 1939, An Introduction to the Study of Stellar Structure (New York: Dover), chap. 10

Chen, X., Abramowicz, M. A., & Lasota, J.-P., 1997, ApJ, 476, 61

Fishbone, L. G., & Moncrief, V. 1976, ApJ, 207, 962

Gammie, C.F., & Popham, R. 1997, ApJ, in press (astro-ph/9705117)

Maxwell, J.C. 1867, Phil. Tran. Roy. Soc. Lon., 157, 49

Muchotrzeb, B., & Paczyński, B. 1982, Acta Astronomica, 32, 1

Nakamura, K. E., Matsumoto, R., Kusunose, M, & Kato, S. 1996, PASJ, 48, 761

Nakamura, K. E., Kusunose, M, Matsumoto, R., & Kato, S. 1997, PASJ, 49, 503

Narayan, R. 1997, in Proceedings of IAU Colloquium 163, Accretion Phenomena and
    Related Objects, A. S. P. Conference Series, eds. D. T. Wickramasinghe, L. Ferrario,
    & G. V. Bicknell, p.75 (astro-ph/9611113)

Narayan, R., Kato, S., & Honma, F. 1997, ApJ, 476, 49

Narayan, R., Loeb, A., & Kumar, P. 1994, ApJ, 431, 359

Narayan, R., Mahadevan, R., Grindlay, J. E., Popham, R. G., & Gammie, C. 1998, ApJ,
    492, 554

Narayan, R., & Yi, I. 1994, ApJ, 428, L13

Narayan, R., & Yi, I. 1995, ApJ, 452, 710

Novikov, I., & Thorne, K.S. 1973, in Black Holes, ed. DeWitt, C. & Dewitt, B.S., (New
    York: Gordon & Breach), p. 343

Paczyński, B., & Bisnovatyi-Kogan, G. 1981, Acta Astronomica, 31, 283

Paczyński, B., & Wiita, P. 1980, A&A, 88, 23

Papaloizou, J.C.B., & Pringle, J. E. 1984, MNRAS, 208, 721

Papaloizou, J.C.B., & Szuszkiewicz, E. 1994, MNRAS, 268, 29

Peitz, J., & Appl, S. 1997, MNRAS, 286, 681 (PA)

Rees, M., Begelman, M.C., Blandford, R.D., & Phinney, E.S. 1982, Nature, 295, 17
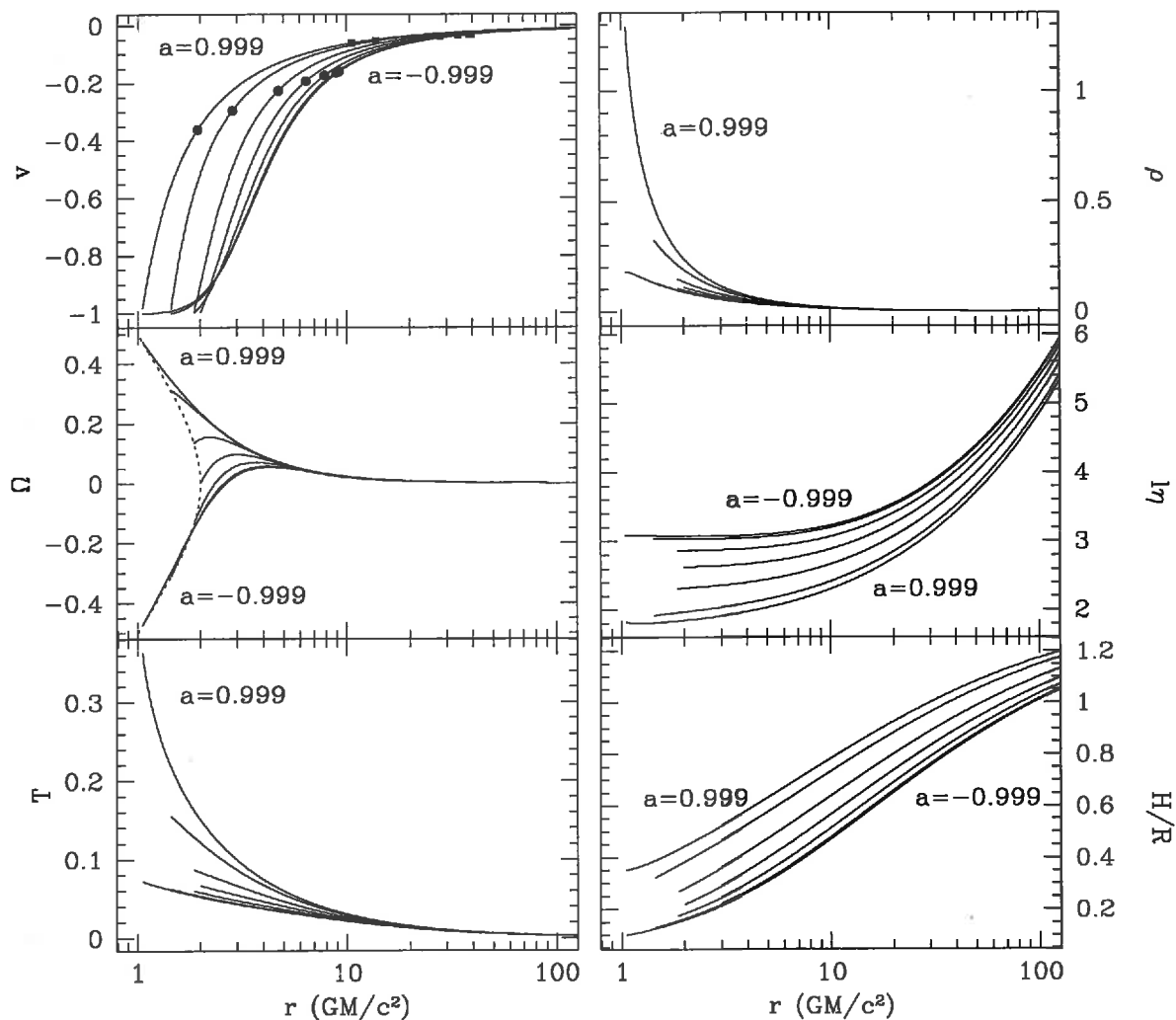
Thorne, K.S. 1974, ApJ, 191, 507

Fig. 1.— Advection-dominated accretion flows for various values of a, all with $\alpha = 0.1$, $f = 1$, and $\gamma = 1.4444$. The solutions shown have $a = -0.999$, -0.9, -0.5, 0, 0.5, 0.9, and 0.999. The six panels show the radial velocity V, density ρ, angular velocity Ω, specific angular momentum $l\eta$, temperature T, and vertical scale height as a fraction of radius H/R. On the panel showing V, the position of the sonic point is denoted by a filled circle, and that of the viscous point by a filled square. On the panel showing Ω, the value of ω at the horizon is given by a dashed line.
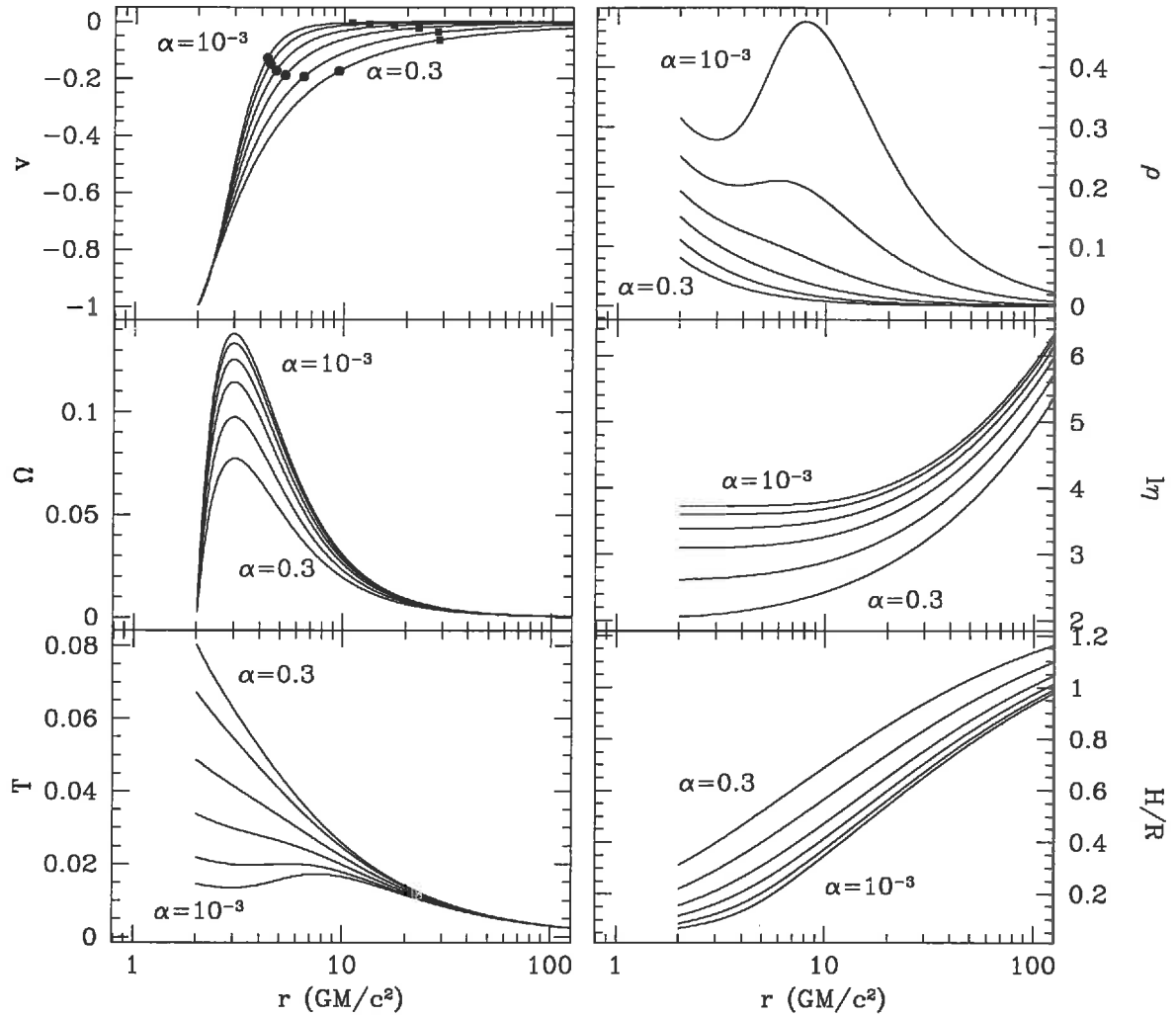
Fig. 2.— Similar to Fig. 1, but for flows with $\alpha = 0.001$, 0.003, 0.01, 0.03, 0.1, and 0.3, all with $a = 0$, $f = 1$, and $\gamma = 1.4444$.
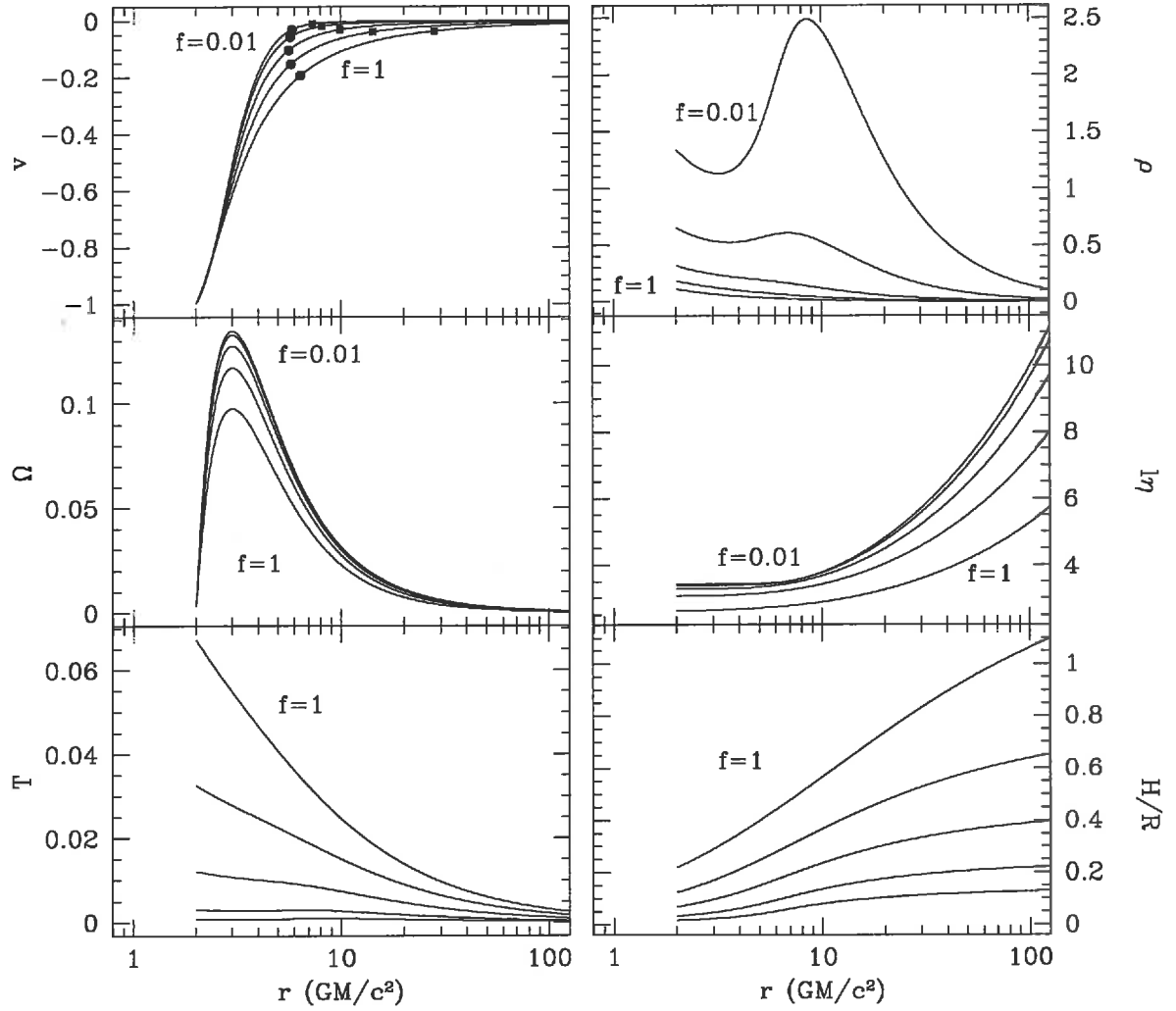
Fig. 3.— Similar to Fig. 1, but for flows with $f = 0.01$, 0.03, 0.1, 0.3, and 1, all with $a = 0$, $\alpha = 0.1$, and $\gamma = 1.4444$.
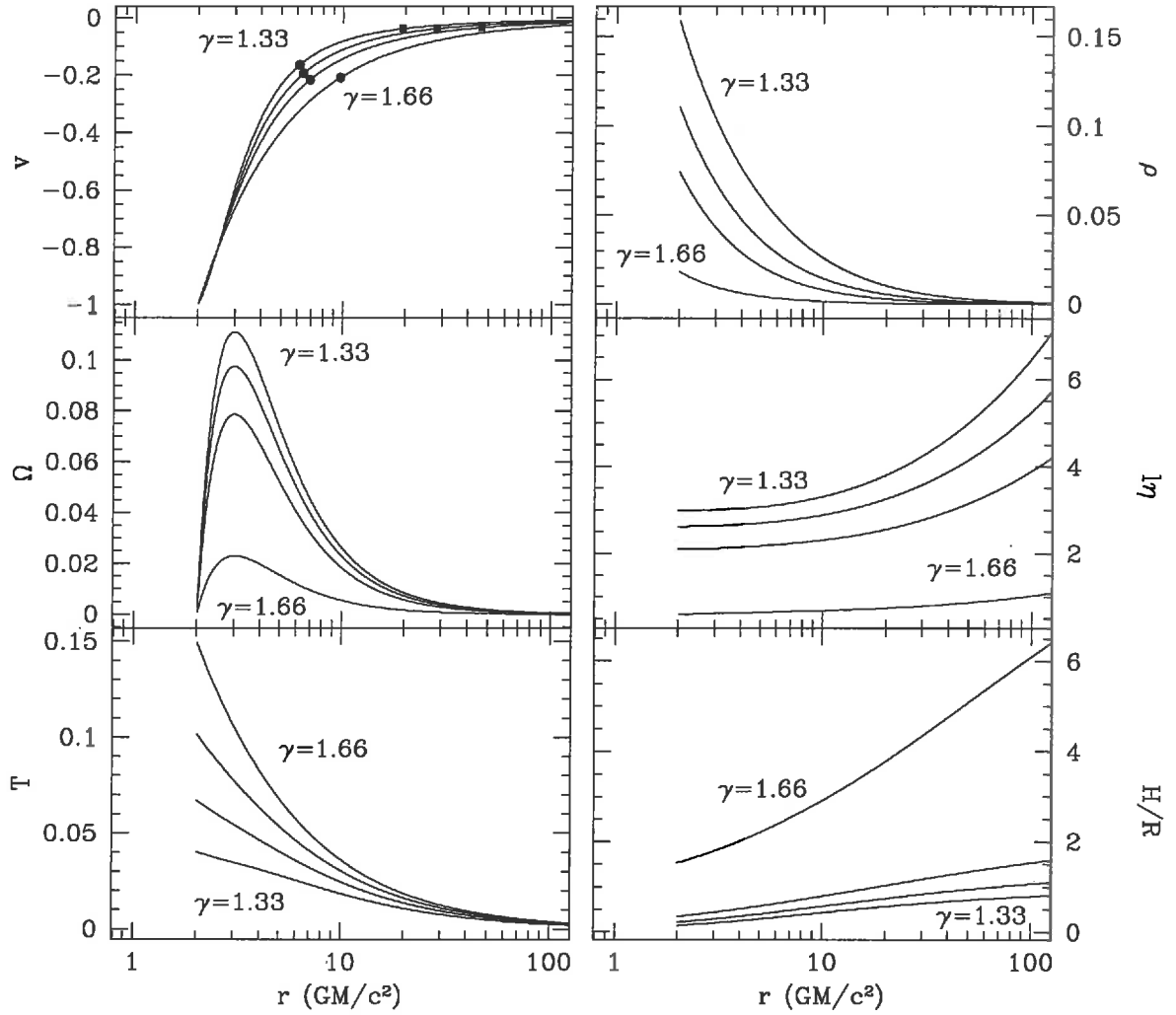
Fig. 4.— Similar to Fig. 1, but for flows with $\gamma = 1.3333$, 1.4444, 1.55, and 1.66, all with $a = 0$, $\alpha = 0.1$, and $f = 1$.
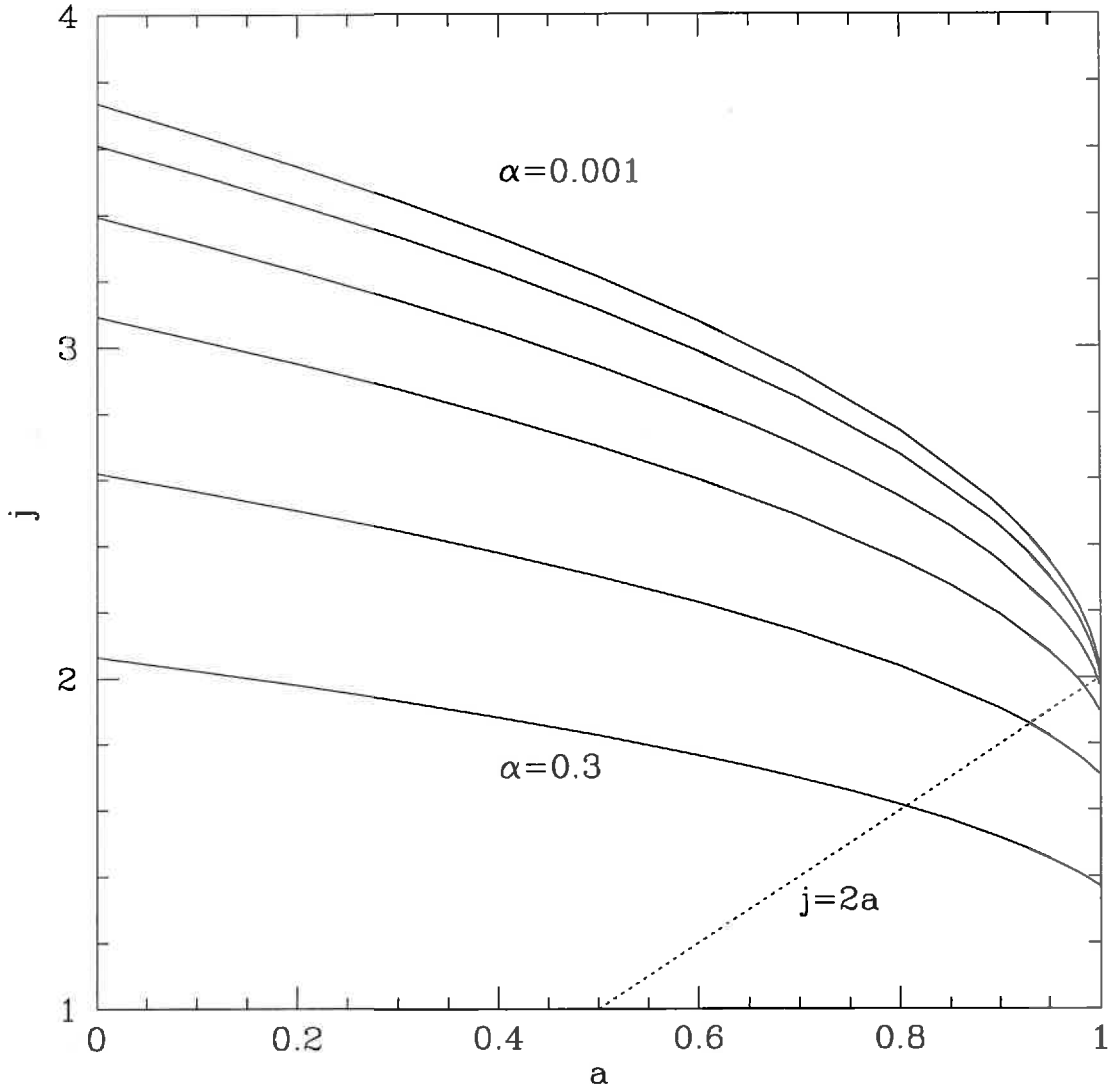
Fig. 5.— (a) The angular momentum accretion rate j as a function of the black hole spin a, for $\alpha = 0.001$, 0.003, 0.01, 0.03, 0.1, and 0.3, all with $f = 1$ and $\gamma = 1.4444$. The dashed line denotes $j = 2a$; for solutions with $j > 2a$, accretion spins up the black hole to larger a. (b) same as (a), but for $f = 0.01$, 0.03, 0.1, 0.3, and 1, all with $\alpha = 0.1$ and $\gamma = 1.4444$.
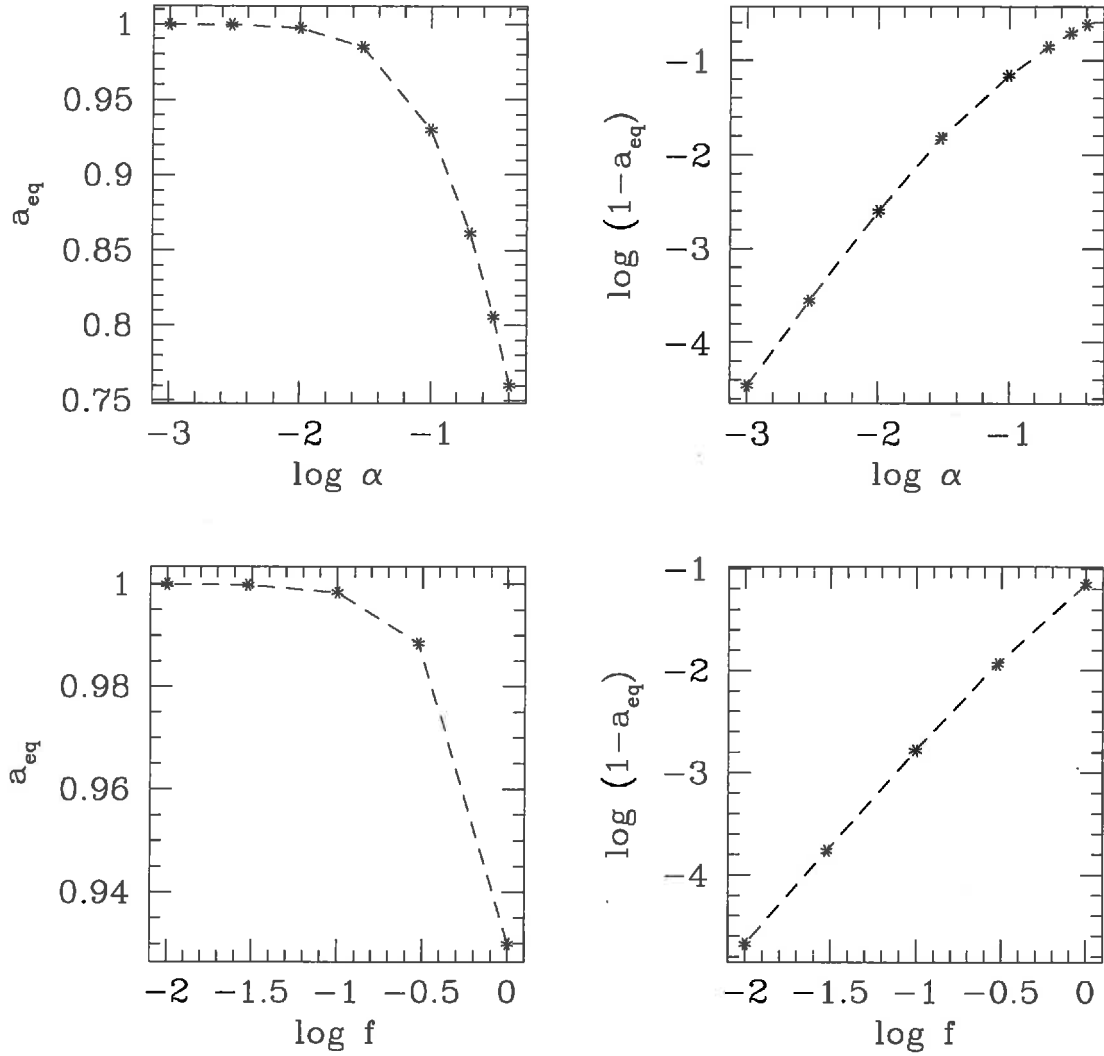
Fig. 6.— The equilibrium value a_{eq}, where $j = 2a$, as a function of α (top panels) and f (bottom panels). The left panel in each case shows a_{eq}, while the right panel shows $\log(1 - a_{eq})$.
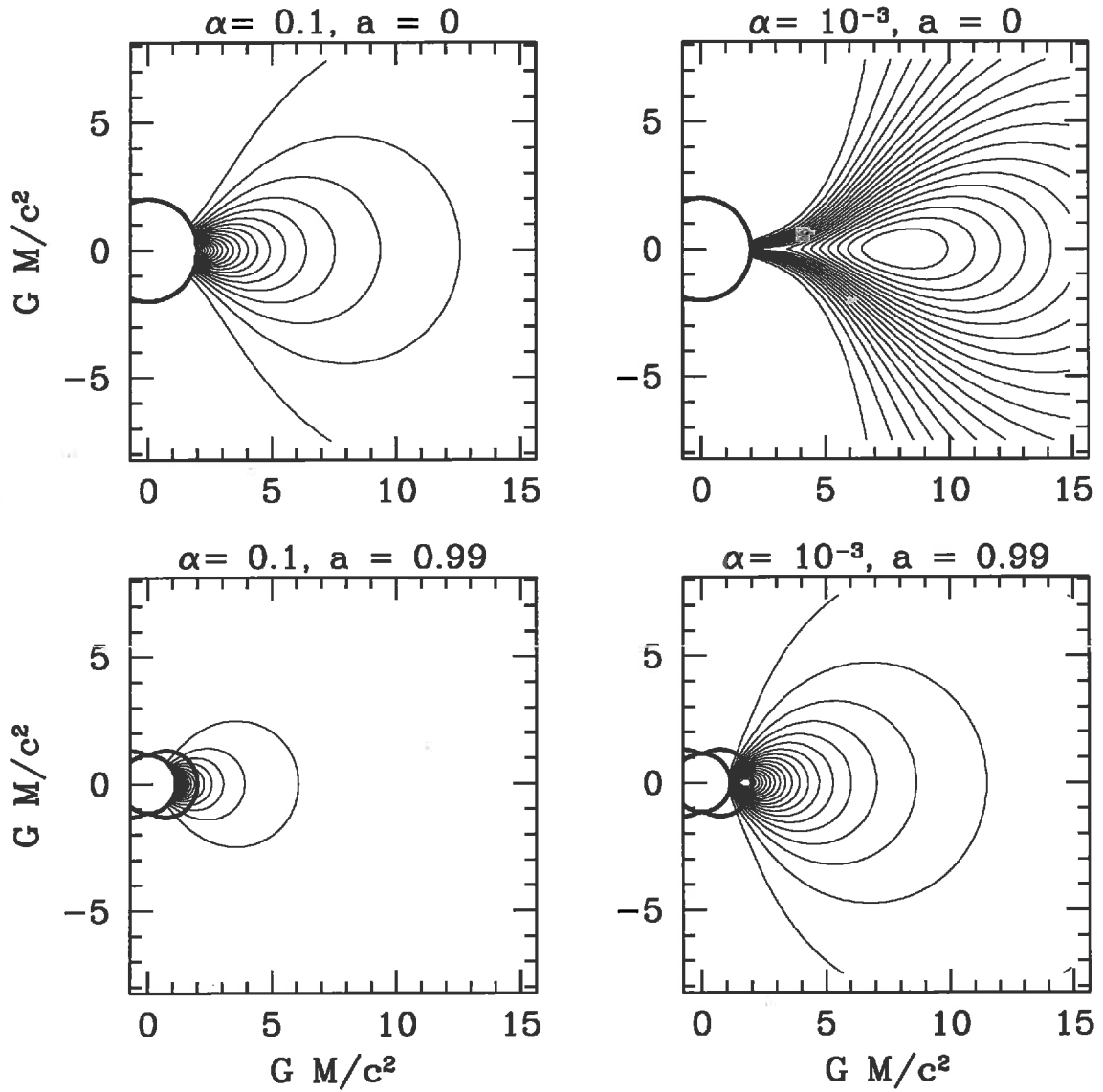
Fig. 7.— The light lines show isodensity contours in the $\varpi = r \sin\theta$, $z = r \cos\theta$ plane, where r, θ are the usual Boyer-Lindquist coordinates. Solutions are shown for $\alpha = 0.1, 10^{-3}$ and $a = 0, 0.99$. The heavy solid lines show the event horizon (inner curve) and the boundary of the ergosphere (outer curve).
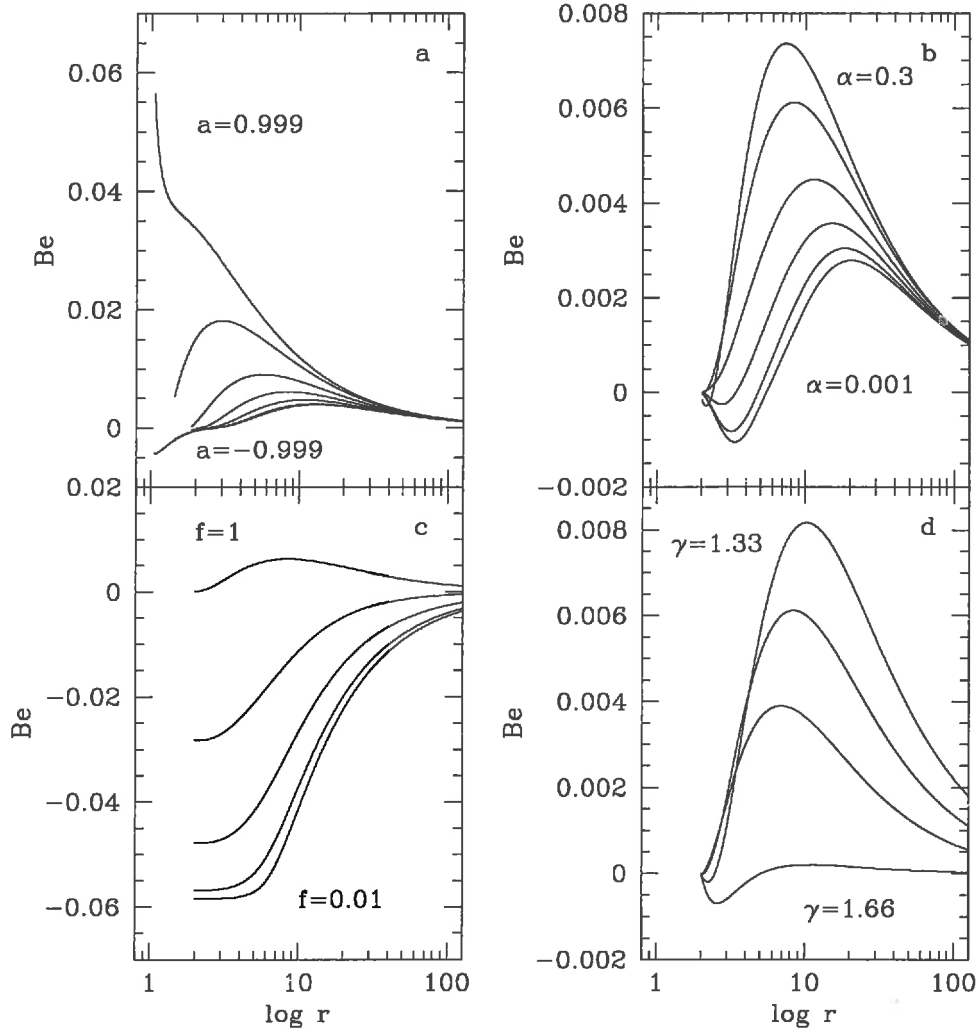
Fig. 8.— The Bernoulli parameter $Be = \eta\mathcal{E} - 1$ as a function of radius for the four sets of solutions shown in Figs. 1-4. The four panels show solutions for various values of (a) a, (b) α, (c) f, and (d) γ.
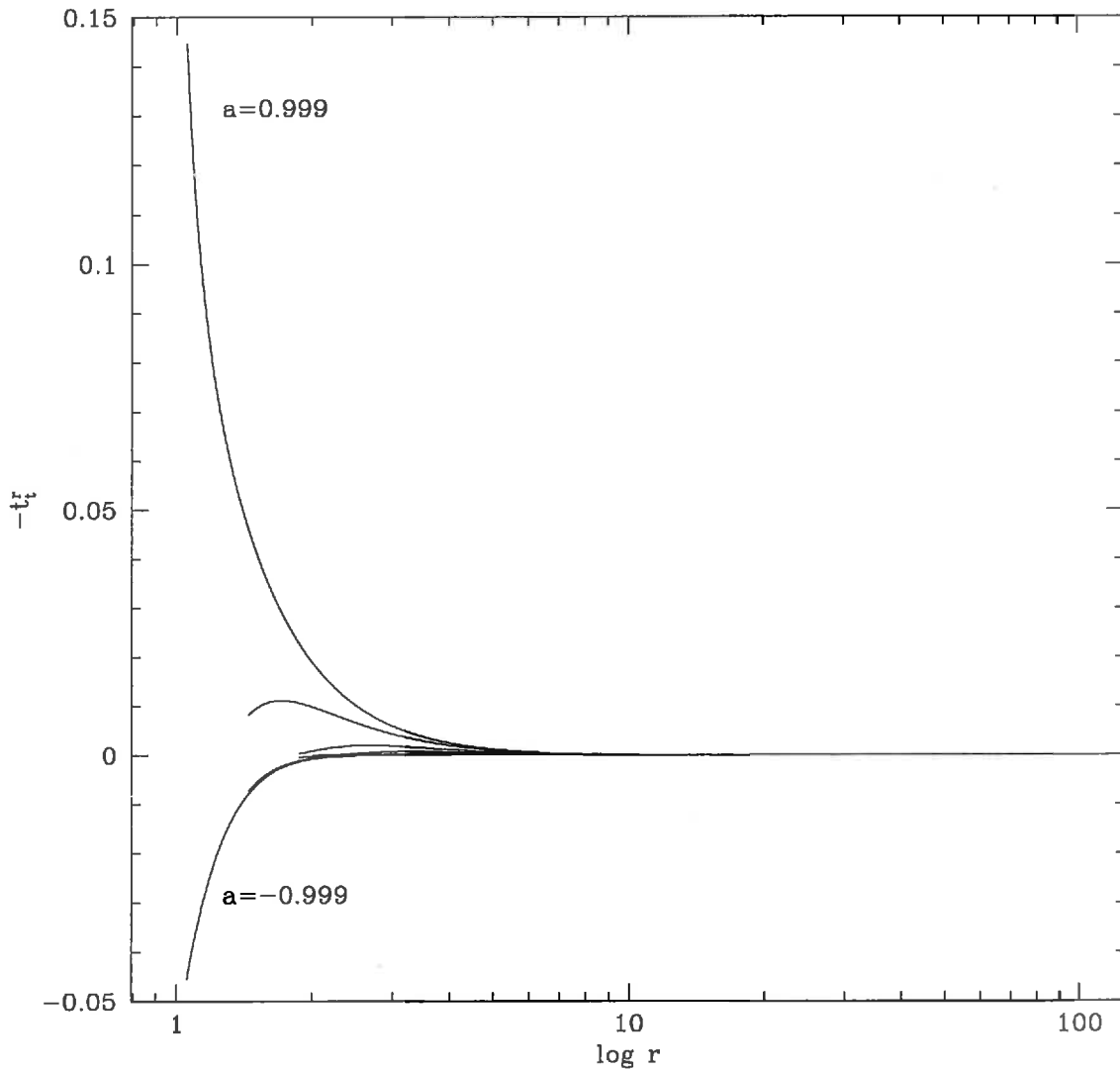
Fig. 9.— The outward viscous energy flux, $-t^r_t$, for solutions with $a = -0.999$, -0.9, -0.5, 0, 0.5, 0.9, 0.999 and otherwise standard parameters. Notice that for $a \gtrsim 0.7$ there is an outward viscous energy flux at the horizon.

Recent Newton Institute Preprints

NI97025-NQF **P van Baal**
Intermediate volumes and the role of instantons

NI97026-NQF **CJ Houghton, NS Manton and PM Sutcliffe**
Rational maps, monopoles and skyrmions
hep-th/9705151; Nuclear Physics B510 [PM] (1998) 507-537

NI97027-NQF **PS Howe, E Sezgin and PC West**
Aspects of superembeddings
hep-th/9705903

NI97028-NQF **CM Hull**
Gravitational duality, branes and charges
hep-th/9705162; Nucl.Phys. B509 (1998) 216-251

NI97029-NQF **M Abou Zeid and CM Hull**
Instrinsic geometry of D-branes
hep-th/9704021; Phys.Lett. B404 (1997) 264-270

NI97030-NQF **CP Bachas, MR Douglas and MB Green**
Anomalous creation of branes
hep-th/9705074

NI97031-RAG **M Broué, G Malle and J Michel**
Complex reflection groups, braid groups, Hecke algebras

NI97032-NQF **D Zwanziger**
Renormalization in the Coulomb gauge and order parameter for confinement in QCD

NI97033-NQF **E Shuryak and A Zhitnisky**
The gluon/charm content of the $\eta\prime$ meson and instantons
hep-ph/9706316; Phys.Rev. D57 (1998) 2001-2004

NI97035-RAG **K Magaard and G Malle**
Irreducibility of alternating and symmetric squares

NI97036-STA **N Linden and S Popescu**
On multi-particle entanglement

NI97037-NNM **M Studeny and RR Bouckaert**
On chain graph models for description of conditional independence structures

NI97038-RAG **M Geck and G Malle**
On special pieces in the unipotent variety

NI97039-NNM **SP Luttrell**
A unified theory of density models and auto-encoders
DERA report DERA/CIS/CIS5/651/FUN/STIT/5-4 31 October 1997

NI97040-NNM **CKI Williams and D Barber**
Bayesian Classification with Gaussian Processes

NI97041-NNM **TS Richardson**
Chain graphs and symmetric associations

NI97042-NNM **A Roverato and J Whittaker**
An importance sampler for graphical Gaussian model inference

NI97043-DQC **MR Haggerty, JB Delos, N Spellmeyer et al**
Extracting classical trajectories from atomic spectra

NI97044-DQC **S Zelditch**
Large level spacings for quantum maps in genus zero

NI97045-DQC **U Smilansky**
Semiclassical quantization of maps and spectral correlations

NI97046-DQC **IY Goldscheid and BA Khoruzhenko**
Distribution of Eigenvalues in non-Hermitian Anderson models
Phys. Rev. Lett. 80 (1998) No.13, 2897-2900

NI97047-DQC	**G Casati, G Maspero and DL Shepelyansky** *Quantum fractal Eigenstates*
NI98001-STA	**N Linden and S Popescu** *Non-local properties of multi-particle density matrices*
NI98002-AMG	**J-L Colliot-Thélène** *Un principe local-global pour les zéro-cycles sur les surfaces fibrés en coniques au-dessus d'une courbe de genre quelconque*
NI98003-AMG	**RGE Pinch and HPF Swinnerton-Dyer** *Arithmetic of diagonal quartic surfaces, II*
NI98004-AMG	**DR Heath-Brown** *The solubility of diagonal cubic diophantine equations*
NI98005-AMG	**B Poonen and M Stoll** *The Cassels-Tate pairing on polarized Abelian varieties*
NI98006-AMG	**P Parimala and V Suresh** *Isotropy of quadratic forms over function fields of curves over p-adic fields*
NI98007-AMG	**E Peyre** *Application of motivic complexes to negligible classes*
NI98008-AMG	**E Peyre** *Torseurs universels et méthode du cercle*
NI98009-RAG	**JA Green** *Discrete series characters for $GL(n,q)$*
NI98010-DQC	**K Zyczkowski** *On the volume of the set of mixed entangled states*
NI98011-DQC	**K Zyczkowski** *Monge distance between quantum states*
NI98012-DAD	**JA Sellwood, RW Nelson and S Tremaine** *Resonant thickening of disks by small satellite galaxies*
NI98013-DAD	**GI Ogilvie and SH Lubow** *The effect of an isothermal atmosphere on the propagation of three-dimensional waves in a thermally stratified accretion disk*
NI98014-DAD	**JA Sellwood and SA Balbus** *Differential rotation and turbulence in extended H I disks*
NI98015-DAD	**AM Fridman and OV Khoruzhii** *On nonlinear dynamics of 3D astrophysical disks*
NI98016-DQC	**RE Prange, R Narevich and O Zaitsev** *Quasiclassical surface of section perturbation theory*
NI98017-DQC	**A Sedrakyan** *Edge excitations of an incompressible fermionic liquid in a disorder magnetic field*
NI98018-DAD	**CF Gammie** *Accretion disk turbulence*
NI98019-DAD	**R Popham and CF Gammie** *Advection dominated accretion flows in the Kerr metric: II. Steady state global solutions*
NI98020-DAD	**CF Gammie and R Narayan** *What is the accretion rate in NGC 4258?*
NI98021-DAD	**CF Gammie** *Photon bubbles in accretion disks*
NI98022-DAD	**EC Ostriker, CF Gammie and JM Stone** *Kinetic and structural evolution of self-gravitating, magnetized clouds: 2.5-dimensional simulations of decaying turbulence*